Synthetic trends for BiVO4 photocatalysts: Molybdenum substitution vs. TiO2 and SnO2 heterojunctions

Kontic, R ; Patzke, Greta R

Abstract: The influence of hydrothermal synthesis, thermal post-treatment at 500 °C and Mo content on a series of Bi1-x/3V1-xMoxO4 ($0.02 < x < 0.15$) photocatalysts was investigated for methylene blue (MB) degradation and O2 evolution. As Mo incorporation stabilizes the formation of tetragonal BiVO4 phases, only calcined Bi0.99V0.98Mo0.02O4 compounds showed good photocatalytic performance in MB decomposition. The Mo-induced blue shift of the band gap thus outweighs the positive influence of Mo-induced morphology stabilization and surface reactivity enhancement in Bi1-x/3V1-xMoxO4 materials. Both BiVO4@TiO2 and BiVO4:Mo@TiO2 heterojunction composites with TiO2 particle coatings in the 10 nm range were newly synthesized and displayed improved photocatalytic performance in MB degradation. Comparative studies with SnO2 heterojunctions revealed a superior influence of TiO2 deposition over SnO2 coating on both BiVO4 and Bi1-x/3V1-xMoxO4 oxide substrates. Different synthetic guidelines for BiVO4-based solid solutions and heterojunctions in photocatalytic wastewater treatment and water oxidation are discussed.

DOI: https://doi.org/10.1016/j.jssc.2011.11.050

Synthetic trends for $BiVO_4$ photocatalysts: Molybdenum substitution vs. TiO_2 and SnO_2 heterojunctions

Roman Kontic[a] and Greta R. Patzke*[a]

[a] Institute of Inorganic Chemistry
University of Zurich
Winterthurerstrasse 190
CH-8057 Zurich
Switzerland

Fax: +41 44 635 6802
Tel: +41 44 635 4691
E-mail: greta.patzke@aci.uzh.ch

Abstract

The influence of hydrothermal synthesis, thermal post-treatment at 500 °C and Mo content on a series of $Bi_{1-x/3}V_{1-x}Mo_xO_4$ ($0.02 < x < 0.15$) photocatalysts was investigated for methylene blue (MB) degradation and O_2 evolution. As Mo incorporation stabilizes the formation of tetragonal $BiVO_4$ phases, only calcined $Bi_{0.99}V_{0.98}Mo_{0.02}O_4$ compounds showed good photocatalytic performance in MB decomposition. The Mo-induced blue shift of the band gap thus outweighs the positive influence of Mo-induced morphology stabilization and surface reactivity enhancement in $Bi_{1-x/3}V_{1-x}Mo_xO_4$ materials. Both $BiVO_4$@TiO_2 and $BiVO_4$:Mo@TiO_2 heterojunction composites with TiO_2 particle coatings in the 10 nm range were newly synthesized and displayed improved photocatalytic performance in MB degradation. Comparative studies with SnO_2 heterojunctions revealed a superior influence of TiO_2 deposition over SnO_2 coating on both $BiVO_4$ and $Bi_{1-x/3}V_{1-x}Mo_xO_4$ oxide substrates. Different synthetic guidelines for $BiVO_4$-based solid solutions and heterojunctions in photocatalytic wastewater treatment and water oxidation are discussed.

Keywords

Bismuth vanadate; Molybdenum; Photocatalysts; Nanomaterials; Water oxidation; TiO_2 heterojunctions

1. Introduction

The quest for visible-light-driven oxide photocatalysts as alternatives to TiO_2 has brought forward manifold promising materials, including bismuth containing oxides [1]. Among their various representatives, the ternary Bi-M-O compounds (M = Mo, W, V, Nb and Ta) excel through their versatile chemical and physical properties [2]. $BiVO_4$ in particular has attracted considerable research attention due to its excellent performance as water oxidation catalyst (WOC) and in the decomposition of organic dyes under visible light irradiation [3]. Three modifications of synthetic $BiVO_4$ are known: the tetragonal zircon type and the monoclinic or tetragonal scheelite structures. The transition of the tetragonal scheelite form into the monoclinic scheelite modification of $BiVO_4$ has been observed in the course of various preparative routes, such as solid state reactions [4], aqueous methods [5], hydrothermal treatment [6] or#microwave-assisted processes [7]. Ultrasonic [8] and flame spray [9] synthetic pathways to $BiVO_4$ have furthermore been established.

Although the monoclinic scheelite type has been identified as the catalytically most active pristine $BiVO_4$ species under visible light irradiation, there is still plenty of room for performance optimization, because the net photocatalytic activity of a given oxide material is not only a function of the crystal and electronic structure [10], but also a complex interplay of preparative history, crystallinity, surface area and other tuning parameters [11]. Oxide photocatalysts can be modified in several ways, e.g. with metals, cation or anion substitution or by combination with other oxide materials, and the resulting effects can be differentiated with respect to surface and bulk doping. Whereas loading of oxide materials with metal particles, such as Au, gives rise to surface plasmon resonance [12], structural substitution and solid solution formation [13] can improve band structure, efficient electron-hole separation and the morphological properties of the respective material, such as particle size or shape. Noble metal deposition on $BiVO_4$ has, for example, been realized with Pd, Pt [14] or Ag [15], and the enhanced photocatalytic properties were ascribed to improved light absorption as well as to synergistic adsorption processes. Transition or rare earth metal doping of $BiVO_4$ has been investigated with respect to metal loading, e.g. Cu-$BiVO_4$ [16], Eu/$BiVO_4$ [17], or Y-substitution of $BiVO_4$ which leads to stabilization of the tetragonal phase in $Bi_{1-x}Y_xVO_4$ catalysts for glucose reforming [18].

Another elegant technique to improve the separation of photogenerated electron-hole pairs in semiconductors is the formation of composites with heterojunction interfaces between components with matching band potentials. The resulting electric field improves the separation of charge carriers and enhances their lifetime - and consequently the photocatalytic efficiency of the material.

The catalytic efficiency of p-n heterojunctions has been demonstrated for core-shell $BiVO_4$@Bi_2O_3 microspheres that display enhanced visible-light response with respect to pristine $BiVO_4$ [19]. Other representative examples of $BiVO_4$ connected with binary metal oxides are $BiVO_4$/WO_3 heterojunction electrodes for water oxidation [20] or V_2O_5-$BiVO_4$ heterojunction composites with separate enrichment of electrons and holes that accumulate on the $BiVO_4$ surface due to close VB positions of both components [21].

These intense efforts nevertheless still leave questions open - as detailed below for the strategy of tuning $BiVO_4$ catalysts through molybdenum incorporation. Although the family of $BiMoVO_x$ oxides has attracted intense research interest with respect to their rich structural chemistry [2], surprisingly few studies have been focused on the influence of Mo-doping on the photocatalytic activity of $BiVO_4$. Band gap tuning of $Ca_{1-x}Bi_xV_xMo_{1-x}O_4$ solid solutions was reported to enhance their O_2 evolution performance with respect to $BiVO_4$ [22]. Only recently, the productive effect of molybdenum incorporation on the degradation of methylene blue (MB) by $BiVO_4$:Mo under visible light irradiation was explained through enhanced adsorption affinities of the photocatalyst due to its higher surface acidity [23]. These preceding investigations on $BiVO_4$:Mo are based on the hypothesis that Mo(VI) substitutes V(V) in the monoclinic scheelite-type $BiVO_4$ host lattice [23] and studies on $Bi_{1-x/3}V_{1-x}Mo_xO_4$ ($x = 0 – 0.3$) solid solutions with $x = 0 – 0.3$ were provided as further confirmation [24]. However, there are no structural database entries available for monoclinic Bi(V, Mo)O_4 phases to the best of our knowledge. On the contrary, it has long been established that Mo incorporation into $BiVO_4$ leads to the stabilization of the tetragonal scheelite-type in solid solutions over the entire $Bi_{1-x/3}V_{1-x}Mo_xO_4$ compositional range until an abrupt structural change sets in for the end member $Bi_2(MoO_4)_3$ [25, 26]. This extended solubility of Mo in tetragonal $BiVO_4$ matrices has been widely confirmed in follow-up studies on $Bi_{1-x/3}V_{1-x}Mo_xO_4$ compounds as oxidation catalysts for organic substrates [27] or as candidates for solid electrolytes [28]. Furthermore, a rather high calcination temperature of 800 °C which is significantly above the onset of MoO_3 sublimation (ca. 700 °C) [29] was applied in the synthesis of the proposed monoclinic $BiVO_4$:Mo catalysts [23] - but no quantitative bulk analysis was provided to verify the reported Mo incorporation of 2 at% after thermal treatment [23]. As other studies reported on particle melting around 800 °C [24] and confirm the absence of monoclinic compounds [13] in Bi/V/Mo/O oxide systems, thorough analytical characterizations of doped monoclinic phases are indispensable. The first part of our systematic hydrothermal study is thus focused on synthesis-structure-activity relationships among $BiVO_4$:Mo solid solutions in order to clarify the influence of V/Mo substitution on phase, particle shape, surface area, thermal stability and catalytic performance of the products.

TiO_2 is an excellent component for photocatalytic heterojunctions that can be accessed with a wide variety of preparative methods [30, 31], but the number of reports on $BiVO_4$@TiO_2 heterojunction composites is still quite limited [32, 33]. The efficiency of $BiVO_4$-TiO_2 heterojunctions in benzene decomposition has been linked to the energy difference of the conduction bands that promotes the transfer of photoexcited electrons from $BiVO_4$ into the conduction band of TiO_2 through joint electric fields at the materials interface [33]. Very little is known about $BiVO_4$@SnO_2 coatings that are also attractive targets as indicated by previous reports on efficient FTO/SnO_2/$BiVO_4$ water splitting electrodes [34]. A recent parameter study on the deposition of $BiVO_4$ films on fluorine-doped tin oxide glass slides illustrates the complex interplay of stirring, pH, particle shape and subsequent annealing with respect to the resulting photocurrents [35]. We have thus investigated the influence TiO_2 or SnO_2 coating, respectively, on the photocatalytic performance of $BiVO_4$ and $Bi_{1-x/3}V_{1-x}Mo_xO_4$ materials. The effects of surface tuning vs. substitutional modifications on the performance of the emerging catalysts are differentiated with respect to visible-light-driven decomposition of methylene blue (MB) or water oxidation.

2. Experimental section

2.1. Preparation of $Bi_{1-x/3}V_{1-x}Mo_xO_4$

In a typical synthesis of $BiVO_4$ nanoparticles, 97 mg of $Bi(NO_3)_3 \cdot 5H_2O$ and 18 mg of V_2O_5 were dispersed in water by 10 min of treatment in an ultrasonic bath. The suspension was transferred into a Teflon-lined stainless steel autoclave with a capacity of 15 mL, filling it to 10 mL, and maintained at 220 °C for 24 h, followed by cooling down to room temperature naturally. The product was collected by centrifugation, repeatedly washed with water and dried in air at 80 °C. An analogous procedure was applied for the synthesis of the $Bi_{1-x/3}V_{1-x}Mo_xO_4$ samples where the V_2O_5 was partially replaced by Na_2MoO_4 with a constant 1:1 molar ratio of Bi : (V + Mo) in the reaction mixture. In the following we will refer to the samples as $BiVO_4$_*X*%Mo, where *X* refers to the percentage of V replaced by Mo in the as-synthesized products (cf. Table 1).

2.2. Coating procedures

For TiO_2 coating, 150 mg of the nanoparticles were suspended by ultrasonication in 10 mL of a 1:1 water / ethanol mixture before adding 30 mg TiF_4 to the suspension, followed by stirring in a closed vial at 60 °C for 2 h. For the SnO_2 coating, 150 mg of the nanoparticles were suspended by ultrasonication in 10 mL water at pH 2 (adjusted by diluted HNO_3) before adding 6 mg SnF_2 to the suspension which was then transferred to a Teflon-lined stainless steel autoclave with a capacity of 15 mL and maintained under stirring at 160 °C for 5 h. For

both coating procedures the reaction vessels were cooled down to room temperature naturally and the products were collected by centrifugation, repeatedly washed with water and dried in air at 80 °C.

2.3. Characterization

Powder X-ray diffraction (XRD) patterns were recorded on a STOE STADI P diffractometer in transmission mode (flat sample holders, Ge monochromator and Cu $K_{\alpha 1}$ radiation) equipped with a position sensitive detector. The patterns were refined using the PM2K software starting from the PDF files 83-1700 and 83-1696 [36]. For scanning electron microscopy (SEM), obtained with a LEO 1530 (FEG) microscope with 2 keV electrons, samples were dispersed in ethanol and subsequently deposited on a silicon wafer.#The Brunauer-Emmett-Teller (BET) surface area measurements were performed on a Quantachrome Quadrasorb SI in N_2-adsorption mode. The samples were degassed at 150 °C for over 3 h under vacuum before the nitrogen adsorption measurement. The optical absorption spectra were recorded in reflection mode on a Perkin-Elmer Lambda 650S spectrophotometer with a 150 mm integration sphere. For elemental analysis a small amount of sample was mixed with Teflon powder, pressed into a pellet and analyzed with a 193 nm ArF excimer laser ablation system (Lambda Physik, Göttingen, Germany) coupled to an ICP-MS (DRC II +, Perkin–Elmer, Norwalk, USA). The samples were ablated for 40 s (5 Hz, 60 μm crater diameter). Transmission electron microscopy (TEM) investigations were performed on a Tecnai F30 ST (FEG, 300kV). Raman spectroscopy was performed on a Renishaw Ramascope 1000 with a green SpectraPhysics Argon laser with a wavelength of 524.5 nm and 50 mW capacity.

2.4. Photocatalytic measurements

For methylene blue (MB) photodegradation experiments 50 mg of the catalyst was dispersed in MB solution (150 mL, 5 ppm) by a ten minutes ultrasonic treatment. The reaction vessel was thermostated at 25 °C with a water cooling jacket; an air flow (100 mL/min) ensured a constant O_2 concentration of the stirred suspension; 10 light bulbs (Osram Dulux S 67 blue, emission maximum at 450 nm, spectrum cf. Fig. S1) were arranged around the photoreactor vessel in a circular fashion. At given time intervals 1.5 mL of the suspension was collected, the catalyst separated by centrifugation and the solution analyzed by recording the change of the MB main peak with a Perkin-Elmer Lambda 650S spectrophotometer with a 150 mm integration sphere.

Photocatalytic O_2 evolution was carried out in a 20 mL headspace vial (with aluminium crimp cap and rubber septum, BGB Analytik, Switzerland) equipped with a stirring bar and filled with a suspension of 10 mg of the catalyst in 13 mL $Fe(NO_3)_3$ solution (10 mmol/L). The

suspension was purged with He to remove all the remaining oxygen from the solvent. The light source was a 476 nm high-flux LED from Rhopoint Components Ltd. (OTLH-0010-BU) with a CPC reflector for Shark LED, operated at usually 4650 lux respectively using a TES 1332A digital lux meter. In regular intervals 100 µL of the reaction headspace were sampled with a gas tight microliter syringe (Hamilton 1825 RN) using a gas chromatograph (Varian CP-3800) with He as carrier gas and a 3 m × 2 mm column packed with molecular sieve 13X 80-100. The gas flow was set to 20 mL/min. The oven was operated isothermally at 100 °C. The gases were detected using a thermal conductivity detector (Varian) operated at 150 °C. Calibrations were performed by the injection of known quantities of pure oxygen diluted in a head space vial containing the same volume of solvent as used for measurements.

3. Results and discussion

3.1. Hydrothermal synthesis, characterization and photocatalytic performance of $Bi_{1-x/3}V_{1-x}Mo_xO_4$ materials

$Bi_{1-x/3}V_{1-x}Mo_xO_4$ compounds were hydrothermally synthesized to shed light on the complex relationships of Mo incorporation and phases together with particle morphology and surface area as key parameters for photocatalytic activity. We investigated whether the previously postulated incorporation of Mo into pure monoclinic $BiVO_4$ matrices [23] can be realized with "soft" hydrothermal methods that might favor these metastable products. Given that DFT studies predict a productive influence of Mo on the conductivity of $BiVO_4$ [37] and that $BiVO_4$:Mo (2 atom%) was reported to exhibit no significant band gap difference to $BiVO_4$ [23], the influence of increasing Mo contents on the band gap of the hydrothermally synthesized compounds was determined. Finally, the interplay of Mo-induced morphology and surface properties in $BiVO_4$ hosts vs. the crystallographic stabilization of the less active tetragonal scheelite form is discussed.

Firstly, a series of mixed $Bi_{1-x/3}V_{1-x}Mo_xO_4$ ($0.02 < x < 0.15$) oxides was obtained from the hydrothermal reaction of $Bi(NO_3)_3 \cdot 5H_2O$, V_2O_5 and Na_2MoO_4. Mo contents before and after thermal treatment were determined with LA-ICP-MS analyses to newly quantify the extent of Mo incorporation [23]. The analytically determined degree of Mo incorporation in the as-synthesized products agrees well with the initial Mo content (Table 1). Furthermore, calcination at 500 °C, i.e. well below the onset of MoO_3 sublimation, does not lead to significant Mo loss over the investigated compositional range.

Table 1. Initial vs. analytically determined compositions of the $Bi_{1-x/3}V_{1-x}Mo_xO_4$ series (values for as-synthesized and calcined samples).

Initial Mo %	Mo % (found) (as-synth.)	Composition	Abbreviation	Mo % (calcined)
2	2.1	$Bi_{0.99}V_{0.98}Mo_{0.02}O_4$	$BiVO_4$_2%Mo	2.1
5	4.0	$Bi_{0.98}V_{0.96}Mo_{0.04}O_4$	$BiVO_4$_4%Mo	4.0
10	7.7	$Bi_{0.97}V_{0.92}Mo_{0.08}O_4$	$BiVO_4$_8%Mo	7.4
15	10.8	$Bi_{0.96}V_{0.89}Mo_{0.11}O_4$	$BiVO_4$_11%Mo	10.3
20	15.1	$Bi_{0.95}V_{0.85}Mo_{0.15}O_4$	$BiVO_4$_15%Mo	13.9

The characteristic region between 28° and 36° θ of the PXRD patterns of as-synthesized and calcined $Bi_{1-x/3}V_{1-x}Mo_xO_4$ ($0 < x < 0.15$) samples is displayed in Fig. 1. Whereas as-synthesized pristine $BiVO_4$ consists mainly of the monoclinic scheelite phase, the amount of the tetragonal modification increases continuously with the Mo content of the samples as expected from preceding solid state studies [25].

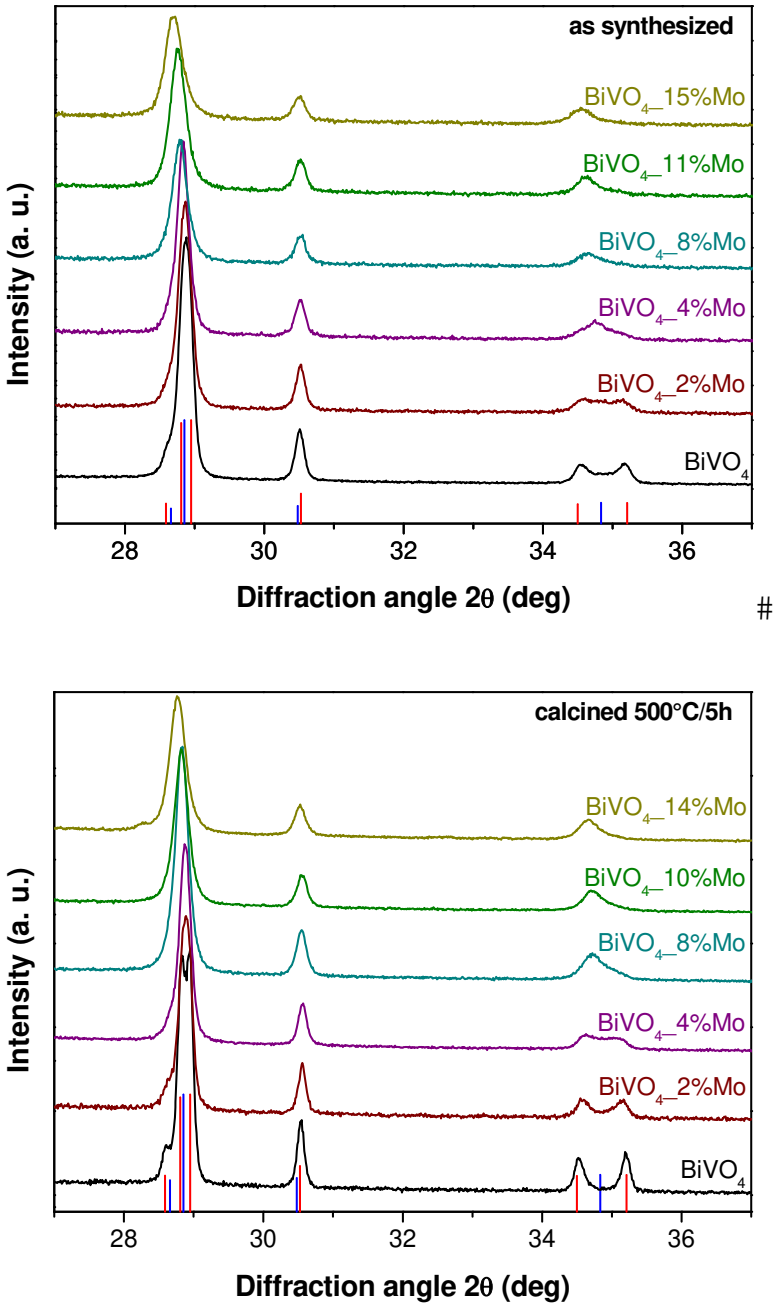

Fig. 1. PXRD patterns of the as synthesized (top) and the calcined (bottom) $Bi_{1-x/3}V_{1-x}Mo_xO_4$ samples. Reference patterns of the monoclinic (red, PDF 83-1700) and tetragonal (blue, PDF 83-1696) scheelite structure of $BiVO_4$ are displayed below.

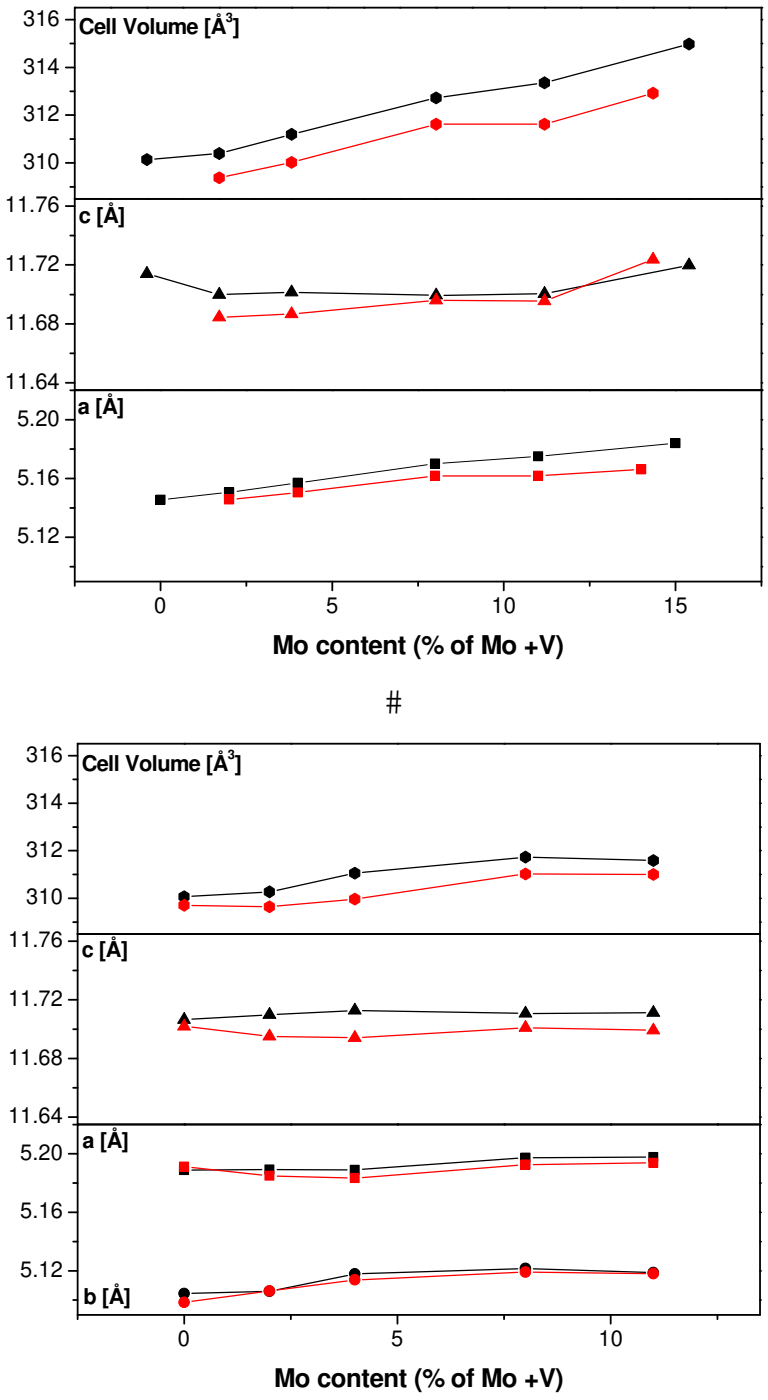

Fig. 2. Lattice parameters (black = as-synthesized, red = calcined) for the tetragonal $BiVO_4$ phase (top) and for the monoclinic $BiVO_4$ phase (below).

Significant amounts of monoclinic scheelite are present in the $BiVO_4$, $BiVO_4$_2%Mo and $BiVO_4$_4%Mo samples after calcination (Fig. 1, top), whereas the tetragonal modification prevails only at higher Mo contents from $BiVO_4$_8%Mo onwards. At first glance, this appears to indicate that Mo can be incorporated into monoclinic $BiVO_4$ with hydrothermal methods. However, only the lattice constants of the tetragonal phase displayed the expected significant increase with the Mo content [25], whilst the values for the monoclinic phase remained

unchanged (cf. Fig. 2 and Table S1). This indicates that the Mo uptake of monoclinic $BiVO_4$ is negligible in comparison with the formation of tetragonal $Bi_{1-x/3}V_{1-x}Mo_xO_4$ compounds.
The influence of hydrothermal Mo incorporation on the $Bi_{1-x/3}V_{1-x}Mo_xO_4$ particle morphology was newly investigated. Despite the presence of both modifications, all samples display a rather homogeneous particle size distribution as can be seen from the SEM images in Fig. 3.

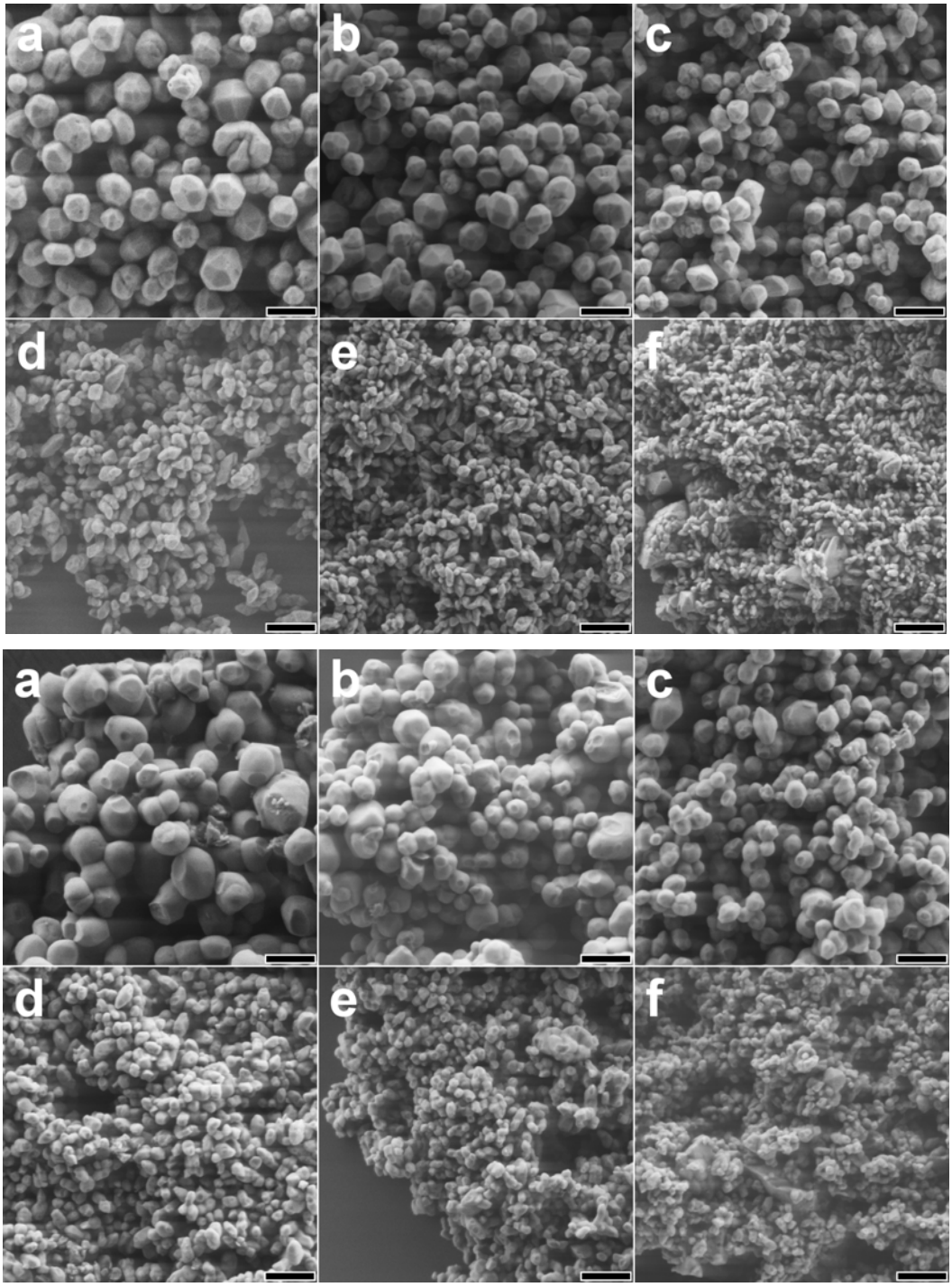

Fig. 3. Representative SEM images showing the influence of increasing Mo content (a: $BiVO_4$, b: $BiVO_4$_2%Mo, c: $BiVO_4$_4%Mo, d: $BiVO_4$_8%Mo, e: $BiVO_4$_11%Mo and f:

$BiVO_4$_15%Mo) on the particle morphology (top: as synthesized, bottom: after calcination (500°C / 5h); scale bar = 400 nm).

The particle size of the as-synthesized materials (Fig. 3, top) decreases continuously with the extent of Mo incorporation from 200 – 400 nm in pristine $BiVO_4$ over 70 – 270 nm in $BiVO_4$_8%Mo to an average particle size of 50 nm in $BiVO_4$_15%Mo. This trend is maintained after calcination (Fig. 3, bottom). Furthermore, increasing Mo contents appear to stabilize the exposition of crystal facets after calcination as can be seen from a comparison of the almost spherical pristine $BiVO_4$ particles (Fig. 3 a, bottom) obtained after heating to 500 °C with the morphologically well-defined calcined $Bi_{1-x/3}V_{1-x}Mo_xO_4$ samples, e.g. $Bi_{0.97}V_{0.92}Mo_{0.08}O_4$ (Fig. 3 d, bottom).

Table 2. BET surface area values (m^2/g) of the as synthesized and coated $Bi_{1-x/3}V_{1-x}Mo_xO_4$ samples before (a) and after (b) calcination (cf. Fig. S2 for a graphical comparison).

Sample	**as-synthesized**		**TiO_2 coated**		**SnO_2 coated**	
	a	**b**	**a**	**b**	**a**	**b**
$BiVO_4$	3.4	3.1	6.0	3.9	7.5	5.6
$BiVO_4$_2 %Mo	3.3	3.3	7.5	4.0	8.5	5.8
$BiVO_4$_4 % Mo	4.4	4.2	9.7	5.9	14.4	8.0
$BiVO_4$_8 %Mo	7.4	7.0	14.3	8.4	18.6	12.1
$BiVO_4$_11 %Mo	10.1	7.0	15.9	8.2	20.5	14.0
$BiVO_4$_15 %Mo	14.4	7.2	20.1	8.1	24.3	15.1

The above-mentioned decrease of particle size upon Mo incorporation goes hand in hand with increasing surface areas (Table 2, left). Lower Mo contents stabilize the particles against calcination, because a significant loss of surface area can only be observed for samples $BiVO_4$_11%Mo and $BiVO_4$_15%Mo. The latter sample furthermore is the only member of the series that displays a significant Mo loss after heating (Table 2) which is likely to induce surface rearrangements. Interestingly, the BET surface area of pristine $BiVO_4$ remains unchanged after calcination although the crystal facets are less pronounced afterwards (Fig. 3 a top/bottom). This illustrates the dual stabilizing influence of moderate V/Mo substitution (up to 5%) on both surface area and particle shape.

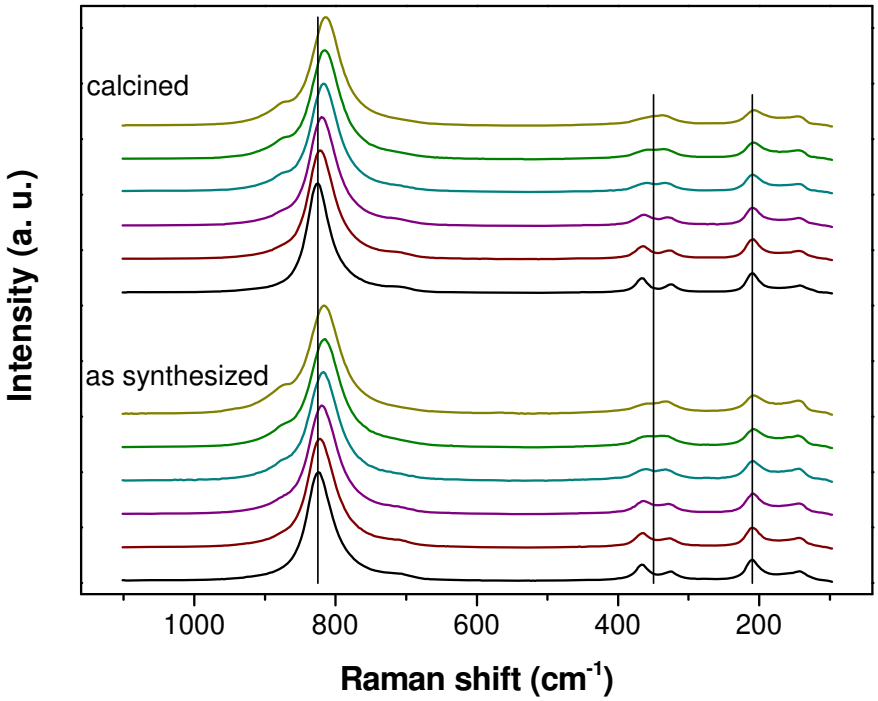

Fig. 4. Influence of the increasing initial Mo content (from black to olive green, same color code as in Fig. 1) on the Raman spectra of as-synthesized and calcined $Bi_{1-x/3}V_{1-x}Mo_xO_4$ samples.

The influence of increasing Mo contents on the Raman spectra of the $Bi_{1-x/3}V_{1-x}Mo_xO_4$ ($0.02 < x < 0.15$) series is evident from Fig. 4: the characteristic symmetric V-O stretching mode (A_g) is shifted from 822 cm^{-1} for as-synthesized pristine $BiVO_4$ to 814 cm^{-1} for $BiVO_4$_15%Mo. Whereas the value for the undoped sample agrees well with literature data (826 cm^{-1}) [7] the observed shift to lower frequencies with increasing content of tetragonal phase among the series is in opposite direction to reference data [38] for the symmetric V-O stretching band of tetragonal $BiVO_4$ at 850 cm^{-1} and can therefore be ascribed to the influence of the Mo content. Generally, this explanation is in line with the previous reports on $BiVO_4$:Mo (2 atom%) [23] and with a peak position around 820 cm^{-1} observed for tetragonal $Bi_{0.85}V_{0.55}Mo_{0.45}O_4$ [28]. In addition, a shoulder near 867 cm^{-1} appears from $BiVO_4$_8%Mo onwards that might be assigned to isolated MoO_4^{2-} tetrahedra which are observed at higher frequencies as shown in key studies on tetrahedral anions [39] as well as in recent investigations on VO_4^{3-} (826 cm^{-1}) vs. MoO_4^{2-} (897 cm^{-1}) moieties in $Mg_{2.5}VMoO_8$ [40]. Monoclinic phase contents are furthermore evident from lower frequency peaks around 371 cm^{-1}, 333 cm^{-1} and 213 cm^{-1} that are in line with the reported values for the symmetric V-O bending (A_g) modes at 365 cm^{-1} and the antisymmetric V-O (B_g) bending mode at 333 cm^{-1}, respectively, as well as with an external mode at 208 cm^{-1} [7]. All peak positions remain practically unchanged upon calcination. The V-O bending modes converge into a single band

which is located at 348 cm^{-1} for the mostly tetragonal $BiVO_4$_15%Mo sample. As the single O-V-O bending mode (A_g) of tetragonal $BiVO_4$ is expected at 380 cm^{-1} from literature data [41], this shift to lower frequencies is likely to arise from Mo incorporation into the crystal lattice, and it follows the trend for the V-O stretching band.

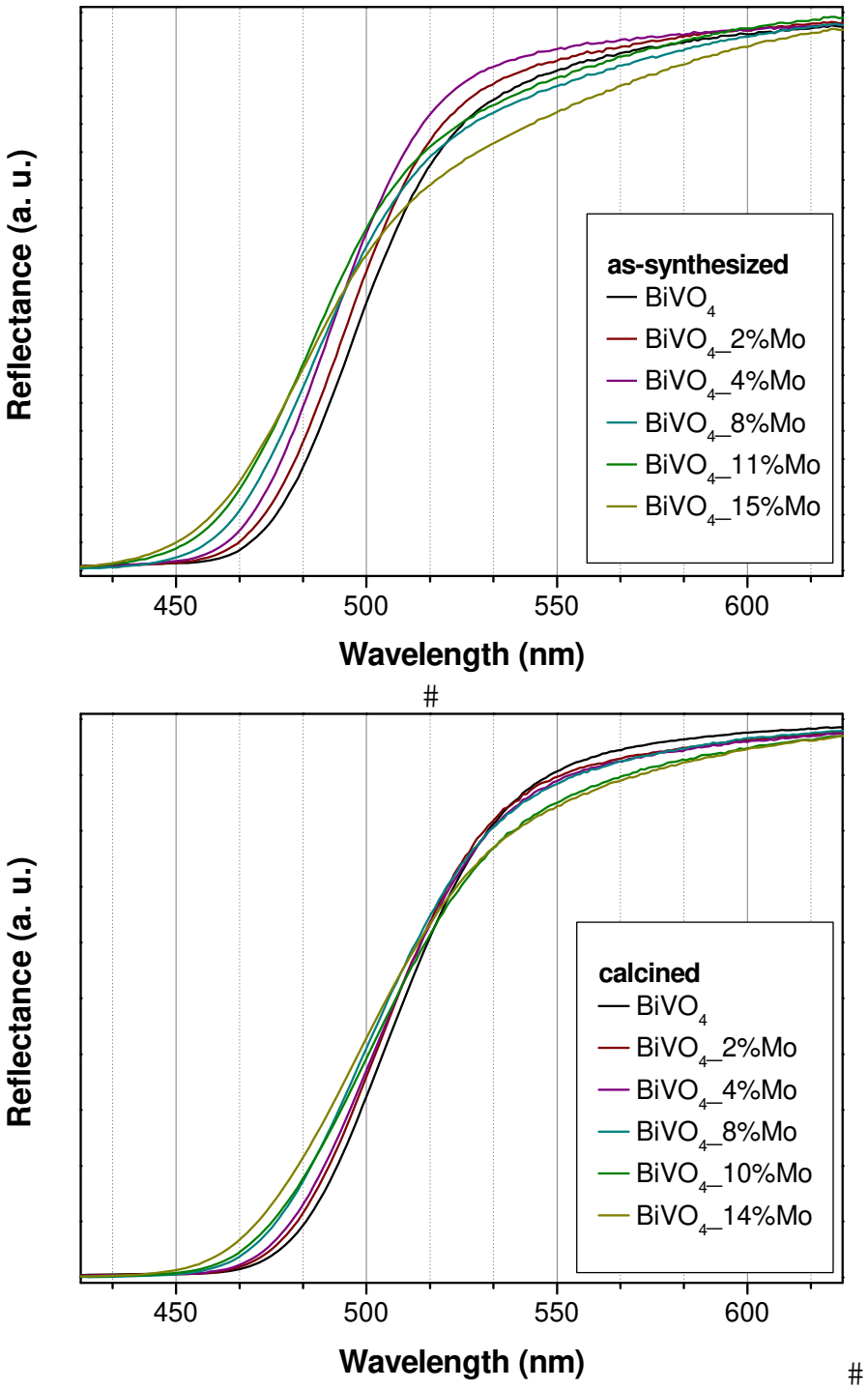

Fig. 5. Comparison of the UV/vis spectra of as-synthesized and calcined $Bi_{1-x/3}V_{1-x}Mo_xO_4$ ($0.02 < x < 0.15$) samples.

Fig. 5 illustrates the influence of increasing Mo contents on the UV/vis spectra of as-synthesized and calcined $Bi_{1-x/3}V_{1-x}Mo_xO_4$ ($0.02 < x < 0.15$) materials. Two trends are emerging for both sample series: higher Mo contents lead to a blue shift of the absorption edge in all samples and calcination slightly decreases the band gap. Concerning pristine $BiVO_4$, this is in line with the reduction of the tetragonal phase content (band gap of 2.9 eV for the tetragonal zircon phase) [7] in favor of monoclinic $BiVO_4$ (band gap 2.4 eV) [7] upon thermal treatment (cf. Fig. 1). Two parameters are involved in the observed blue shift among the $Bi_{1-x/3}V_{1-x}Mo_xO_4$ series, namely the Mo-induced stabilization of the tetragonal phase and a potential influence of Mo substitution on the electronic structure. Interestingly, however, previous experimental studies [22, 23] indicate a productive influence of Mo incorporation into $BiVO_4$ matrices which is probably a more complex phenomenon that cannot be explained in terms of band gap tuning alone.

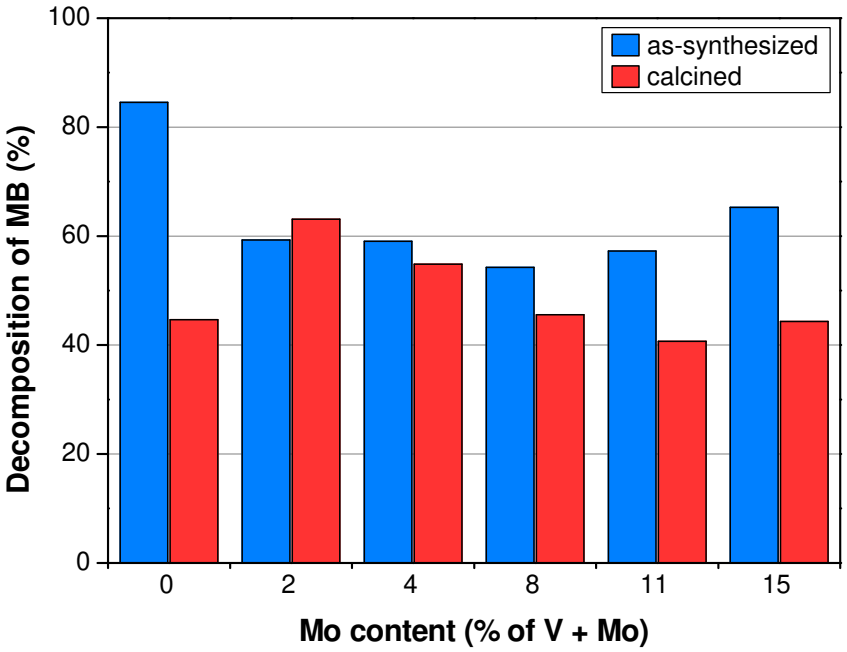

Fig. 6. Methylene blue degradation of as-synthesized and calcined $Bi_{1-x/3}V_{1-x}Mo_xO_4$ samples under visible light irradiation (MB degradation after 2 h).

The photocatalytic performance of the hydrothermally synthesized vs. calcined $Bi_{1-x/3}V_{1-x}Mo_xO_4$ ($0.02 < x < 0.15$) samples is shown in Fig. 6. As-synthesized pristine $BiVO_4$ displays the highest activity in the decomposition of methylene blue (MB) under visible light irradiation and all of the as-synthesized Mo-containing samples are less active. Obviously, the enhanced surface areas of the $Bi_{1-x/3}V_{1-x}Mo_xO_4$ samples and enhanced surface reactivity through Mo centers cannot fully compensate the continuous blue shift of the absorption edge (Fig. 5). At first glance, this suggests a counterproductive influence of Mo on the overall

photocatalytic activity. Interestingly, however, calcination of pristine $BiVO_4$ significantly reduces its photocatalytic activity - despite a narrowing of the band gap, a higher amount of the more active monoclinic phase and unchanged BET surface area in comparison with as-synthesized $BiVO_4$. It is noteworthy that calcined $BiVO_4$_2%Mo and $BiVO_4$_4%Mo exhibit higher photocatalytic activity than calcined $BiVO_4$, although both samples display higher tetragonal phase contents together with blue shifts of the absorption edge and comparable surface areas (Table 2). The performance of the remaining calcined samples ($BiVO_4$_8% to $BiVO_4$_15%Mo) is comparable to pristine calcined $BiVO_4$.

Given that the phase trends among calcined and as-synthesized samples are analogous (cf. PXRD patterns in Fig. 1), the reason for the declined activity of calcined $BiVO_4$ is probably linked to the loss of exposed and reactive crystal facets during calcination as is evident from the comparison of SEM images before (Fig. 3 a, top) and after (Fig. 3 a, bottom) calcination. In comparison, the calcined $Bi_{1-x/3}V_{1-x}Mo_xO_4$ (x = 0.02, 0.04) samples benefit from more pronounced crystal shapes which might also enhance Mo-related surface acidity and reactivity. Given that higher Mo contents may exert an overall deteriorating effect as indicated from the results on as-synthesized products, replacement of 2-5 % V by Mo, followed by calcination under mild conditions (500 °C) is an optimal procedure to generate $Bi_{1-x/3}V_{1-x}Mo_xO_4$ photocatalysts for the decomposition of organic compounds.

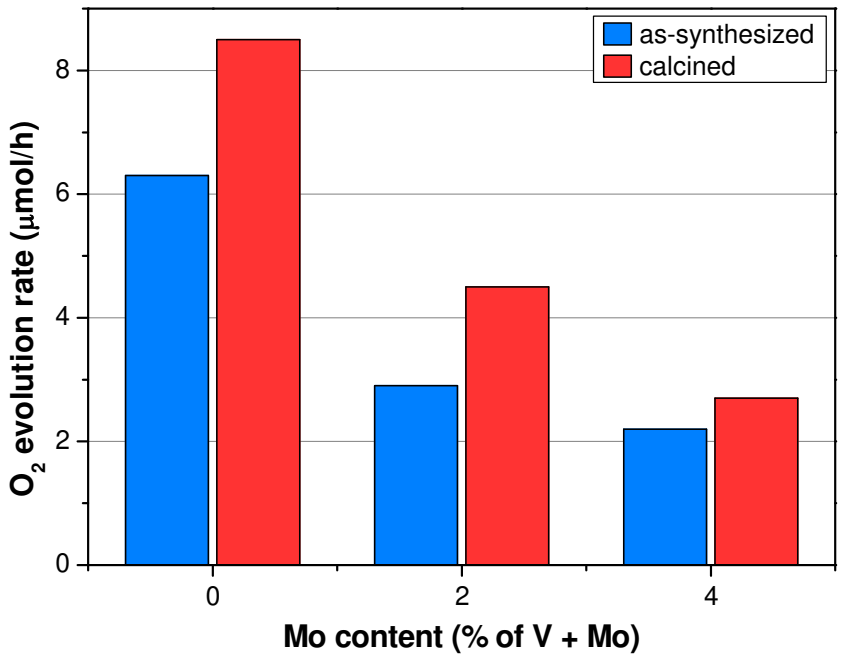

Fig. 7. Comparison of the photocatalytic O_2 production of as-synthesized and calcined $Bi_{1-x/3}V_{1-x}Mo_xO_4$ samples under visible light irradiation.

Fig. 7 compares the photocatalytic O_2 production performance of calcined and as-synthesized $BiVO_4$ to the above selected $Bi_{1-x/3}V_{1-x}Mo_xO_4$ (x = 0.02, 0.04) samples. Other than in MB decomposition, the pristine $BiVO_4$ sample displays enhanced activity after calcination as expected from phase contents and absorption edge trends. In sharp contrast to the aforementioned productive influence of Mo incorporation and calcination on MB degradation (Fig. 6), the O_2 evolution rate of the Mo-containing samples decreases notably in comparison with calcined $BiVO_4$. These observations are fully in line with the UV/vis trends for all catalyst samples as shown in Fig. 5: band gap widening lowers O_2 production efficiency. This agrees with our preceding study on different parameters trends among hydrothermally $BiVO_4$ synthesized particles with respect to MB decomposition and water oxidation: Degradation of organic compounds requires optimized particle morphologies and high surface areas, whereas band gap as well as overall crystallinity are more important for O_2 evolution [42]. Mo(VI) ions are furthermore potential recombination centers that can diminish O_2 production: this may explain the considerable differences between the present results and the previously reported enhanced O_2 evolution performance of $BiVO_4$:Mo [23].

The emerging overall trends for the hydrothermal synthesis of photocatalytic $Bi_{1-x/3}V_{1-x}Mo_xO_4$ ($0.02 < x < 0.15$) materials can be summed up as follows:

• The applied template-free hydrothermal technique starting from $Bi(NO_3)_3 \cdot 5H_2O$, V_2O_5 and Na_2MoO_4, followed by mild thermal post-treatment, is preferable over sintering pathways to $BiVO_4$ based photocatalysts for the degradation of organic compounds, because calcination above 500 °C bears the risk of molybdenum loss and permits less control over morphology and surface area.

• Furthermore, Mo incorporation generally stabilizes the less active tetragonal $BiVO_4$ modification and this effect cannot be circumvented by “soft” hydrothermal strategies. As a consequence, the previously proposed Mo substitution in the local crystal structure of monoclinic $BiVO_4$ catalysts through calcination at 800 °C needs to be revised [23].

• Methodological advantages of hydrothermal synthesis over classic solid state formation of $Bi_{1-x/3}V_{1-x}Mo_xO_4$ materials lie in the decrease of particle size with increasing Mo content (down to 50 nm), accompanied by larger surface areas (max. 14 m^2/g) and, most importantly, enhanced morphological stability of the samples after calcination at 500 °C with respect to pristine $BiVO_4$.

• Despite morphological and surface properties enhancements, the blue shift of the absorption edge for Mo-containing catalysts with respect to pristine $BiVO_4$ still outweighs these benefits. As a result, preceding studies on enhanced O_2 evolution with monoclinic $BiVO_4$:Mo catalysts could not be confirmed [23] and Mo doping of $BiVO_4$ can neither be recommended for MB

degradation nor water oxidation catalysis at the present stage. Calcination of the hydrothermally obtained $BiVO_4$-based catalysts is not essential for MB degradation but increases the O_2 production activity. Only if special thermal post-treatment of catalysts is required, e.g. to guarantee long-term stability under special conditions, moderate hydrothermal V/Mo substitution (up to 4 %) might be productive for the performance improvement of dye degradation with $Bi_{1-x/3}V_{1-x}Mo_xO_4$ photocatalysts.

3.2. Influence of TiO_2 and SnO_2 coating on the photocatalytic performance of $Bi_{1-x/3}V_{1-x}Mo_xO_4$ materials

3.2.1. Coating of $Bi_{1-x/3}V_{1-x}Mo_xO_4$ substrates with TiO_2 nanoparticles

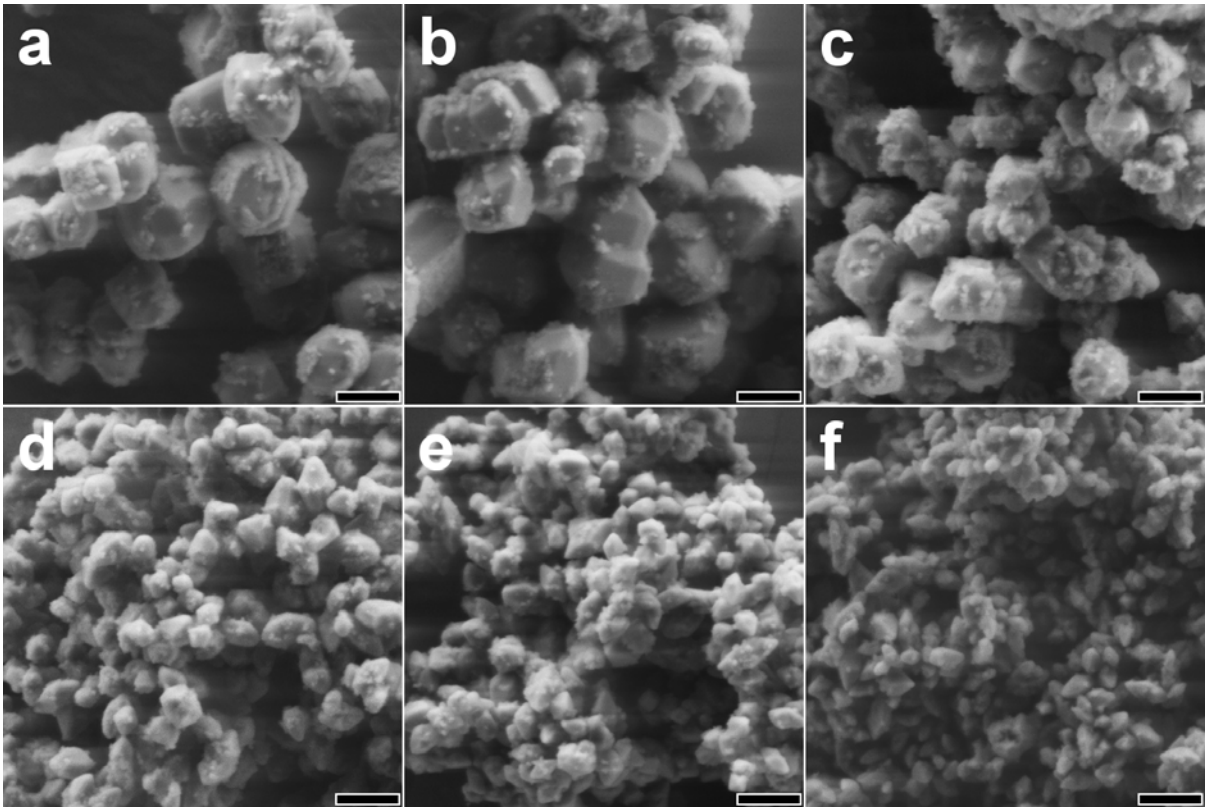

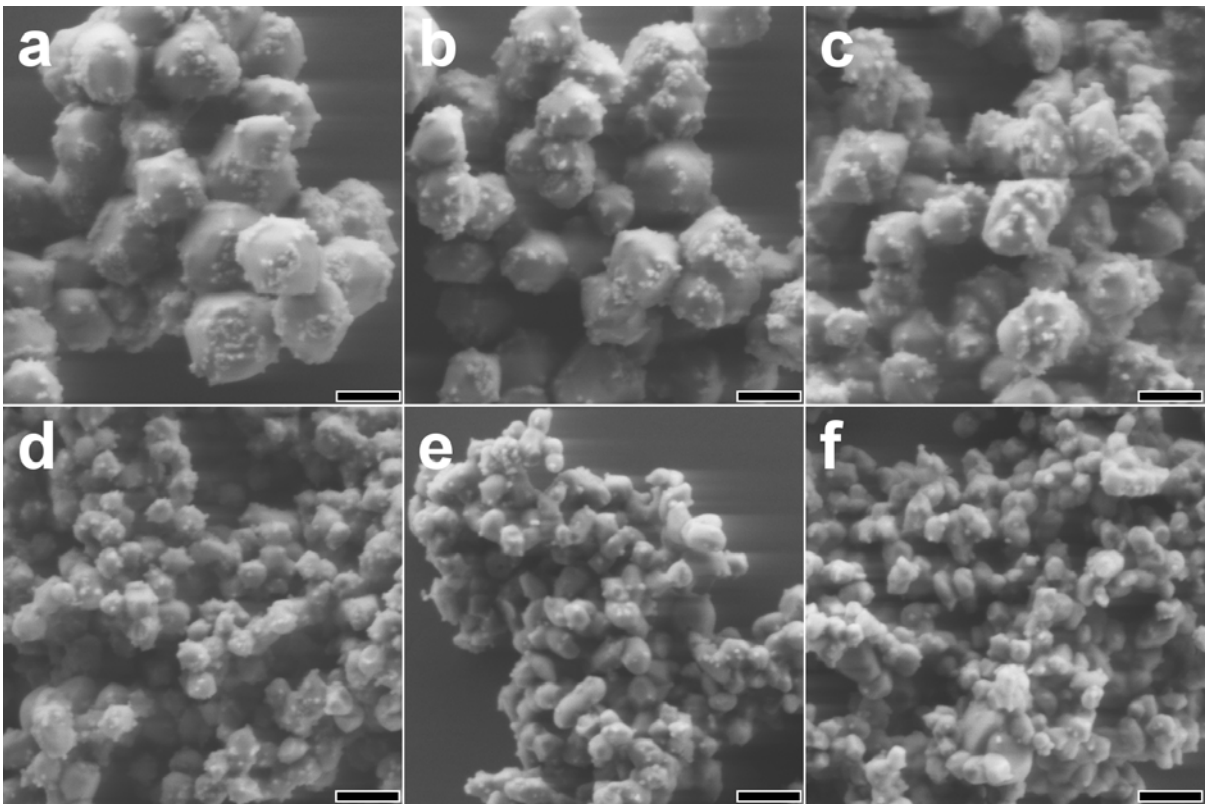

Fig. 8. Representative SEM images of TiO_2 coated $Bi_{1-x/3}V_{1-x}Mo_xO_4$ nanoparticles (a: 0 %, b: 2 %, c: 4 %, d: 8 %, e: 11 % and f: 15 % Mo content), before (top) and after (bottom) calcination (500 °C / 5 h); scale bar = 200 nm.

TiO_2 nanoparticles were deposited on the surface of $BiVO_4$ and $Bi_{1-x/3}V_{1-x}Mo_xO_4$ materials with a mild one-step procedure starting from TiF_4 (cf. experimental section) in order to investigate the effect of nanoscale heterojunction formation on the emerging $BiVO_4$@TiO_2 and $BiVO_4$_X%Mo@TiO_2 (X = 2, 4, 8, 11, 15) products, respectively.

Fig. 8 displays a survey of representative SEM images of the composites before and after calcination at 500 °C for 5 h. The freshly deposited TiO_2 particles have diameters of 10 – 20 nm and they are preferentially deposited on specific crystal facets where their size remains constant after thermal treatment. The degree of coating was too low to permit a differentiation between rutile and anatase in the Raman spectra (cf. Fig. S3) or PXRD patterns. HRTEM investigations (Fig. 9) confirm the small particle size and the crystallinity of the deposited TiO_2 particles as well as the presence of TiO_2-free facets.

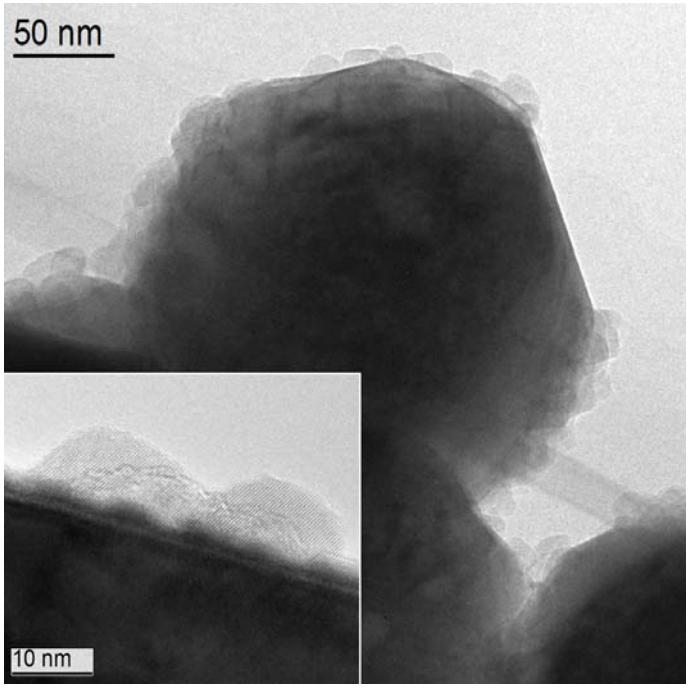

Fig. 9. TEM image of calcined $BiVO_4$:2%Mo@TiO_2 particles (inset: close-up of TiO_2 coating).

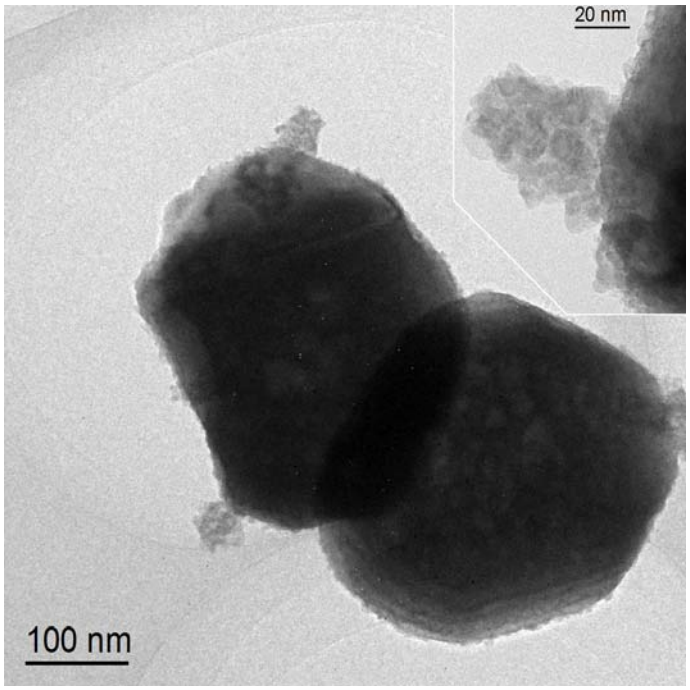

Fig. 10. TEM image of calcined $BiVO_4$:2%Mo@SnO_2 particles (inset: close-up of SnO_2 coating).

TiO_2 coating notably enhances the BET surface area of the as-synthesized composites by a factor of 1.5 to 2 (Table 2). Although these values are basically reduced to those of the pristine oxides after calcination, the morphology and crystal facets of the calcined products

are maintained quite well (Fig. 8, bottom) and this applies especially for $BiVO_4$@TiO_2 in comparison with pristine calcined $BiVO_4$ (Fig. 3 a, bottom).

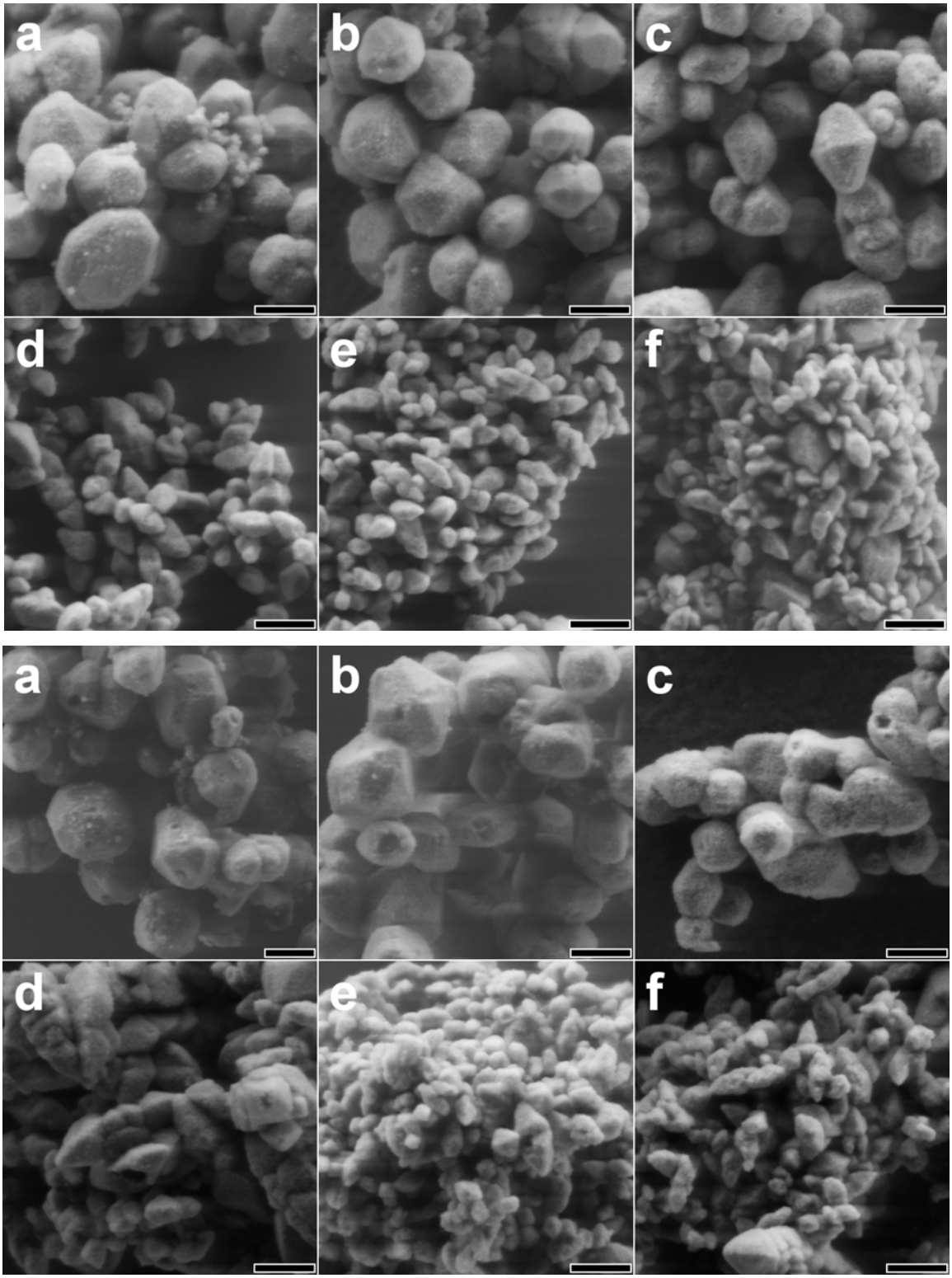

Fig. 11. Representative SEM images of SnO_2 coated $Bi_{1-x/3}V_{1-x}Mo_xO_4$ nanoparticles (a: 0 %, b: 2 %, c: 4 %, d: 8 %, e: 11 % and f: 15 % Mo content), before (top) and after (bottom) calcination (500 °C / 5h); scale bar = 200 nm.

Other than the facile TiO_2 deposition under ambient conditions, hydrothermal treatment was required to obtain SnO_2 coating from the SnF_2 precursor (cf. experimental section). SEM images (Fig. 11) show that the oxide substrates are covered with a dense layer of rather small SnO_2 particles. HRTEM investigations (Fig. 10) demonstrate that their maximum diameters are around 15 nm and that they are distributed without any morphological preferences over the oxide substrate. The presence of Ti and Sn, respectively, on the $BiVO_4$ surface was confirmed with STEM-EDX measurements (Fig. S4 and S5). These characteristics are maintained after calcination so that the bismuth vanadate based core particles are protected against further agglomeration. The BET surface areas of the as-synthesized $BiVO_4$@SnO_2 and $BiVO_4$:_X%Mo@SnO_2 (X = 2, 4, 8, 11, 15) composites exceed those of the TiO_2 analogues as a consequence of the smaller particle sizes and higher coating densities. In contrast to the TiO_2 heterojunctions, the surface enlargement is partially maintained in the SnO_2-based composites after calcination (cf. Table 2). Nevertheless, no indications of SnO_2 were detectable in Raman spectra prior to and after thermal treatment (Fig. S3).

The productive influence of both TiO_2 and SnO_2 coating on calcined pristine $BiVO_4$ samples is illustrated in Fig. 12: the photocatalytic activity in MB degradation is doubled for $BiVO_4$@TiO_2 and $BiVO_4$@SnO_2. The emission spectrum of the blue light lamps used for visible light irradiation shows very little overlap with the absorption spectrum of MB (Fig. S1), hence minimizing the possibility of dye sensitizing of TiO_2. Pristine $BiVO_4$, $BiVO_4$@TiO_2 and $BiVO_4$@SnO_2 samples display the highest catalytic performance in MB degradation, thus confirming the trends observed for as-synthesized and calcined $Bi_{1-x/3}V_{1-x}Mo_xO_4$ samples (Fig. 6). Interestingly, the catalytic activity of the $BiVO_4$ heterojunction compounds is maintained upon calcination and it significantly improves the performance of the $Bi_{1-x/3}V_{1-x}Mo_xO_4$@TiO_2 materials. As observed for the uncoated $Bi_{1-x/3}V_{1-x}Mo_xO_4$ series, the calcined $BiVO_4$_2%Mo@TiO_2 and $BiVO_4$_4%Mo@TiO_2 samples with lower Mo contents display the highest activity and the overall MB decomposition rate decreases again with Mo incorporation. A detailed comparison of XRD patterns of the pristine and calcined $Bi_{1-x/3}V_{1-x}Mo_xO_4$@TiO_2 samples showed slightly enhanced crystallinity (Fig. S6) whilst the BET surface area was generally reduced (Table 2). This points to catalytic performance enhancement through charge carrier separation at the $BiVO_4$/TiO_2 heterojunction interface that are improved through moderate calcination whilst surface area effects and dye sensitization are less influential.

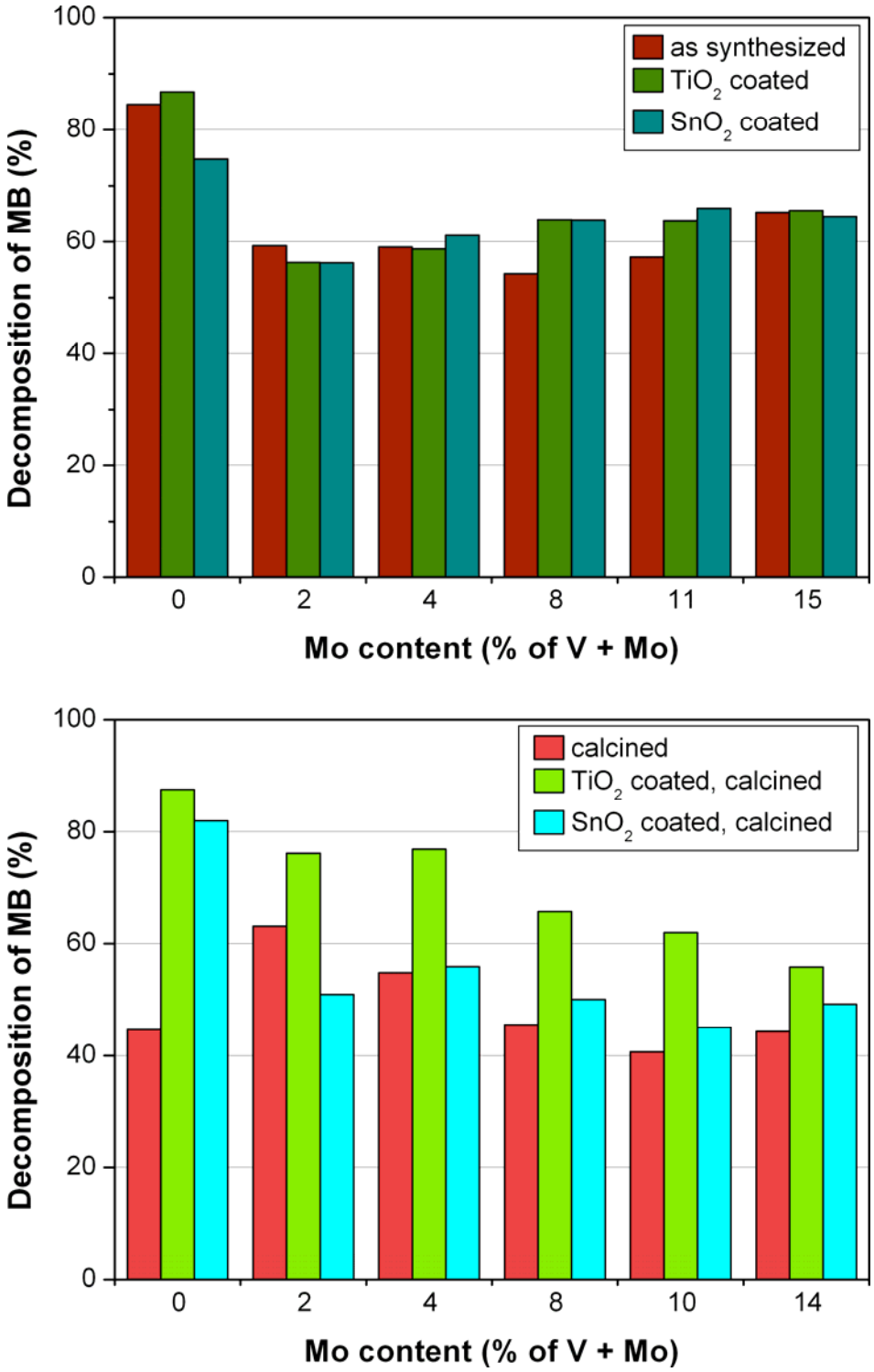

Fig. 12. Methylene blue degradation with TiO_2- or SnO_2-coated pristine (top) and calcined (bottom) $BiVO_4$ and $Bi_{1-x/3}V_{1-x}Mo_xO_4$, respectively, under visible light irradiation (MB degradation after 2 h).

Interestingly, SnO_2 coating and calcination deteriorates the photocatalytic performance of the hitherto most active $BiVO_4$_2%Mo and $BiVO_4$_4%Mo members of the solid solution series. This indicates moderate surface activity and acidity enhancement through 2-4 % Mo doping which is concealed by the dense SnO_2 layer. Other than for TiO_2 coated samples, calcination of the SnO_2 containing composites does not seem to exert a productive effect on

heterojunction formation and the catalytic activity goes down hand in hand with the BET surface (Table 2).

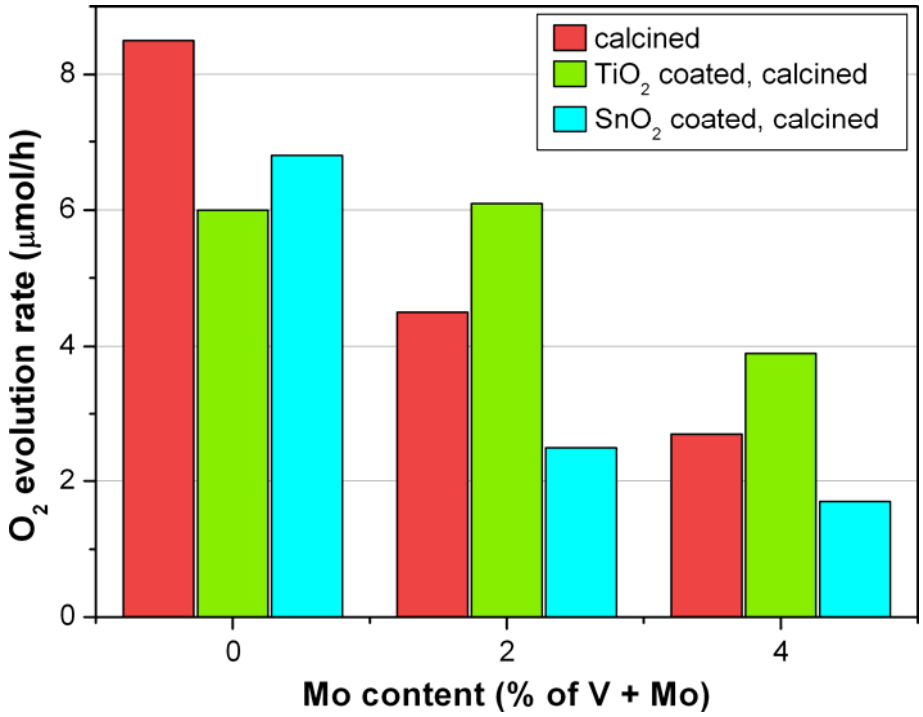

Fig. 13. Comparison of photocatalytic O_2 production of pristine and modified, calcined $Bi_{1-x/3}V_{1-x}Mo_xO_4$ samples under visible light irradiation.

Whereas the O_2 evolution performance (cf. Fig. 13) of both calcined $BiVO_4$@TiO_2 and $BiVO_4$@SnO_2 is lower than for pristine calcined $BiVO_4$, the $BiVO_4$_2%Mo@TiO_2 and the $BiVO_4$_4%Mo@TiO_2 samples display enhanced activities upon coating, albeit not higher than the Mo-free samples. Highly crystalline TiO_2 heterojunctions appear to compensate the adverse effects of possible Mo recombination centers (cf. Fig. 9). The observation that the denser SnO_2 coatings are entirely counterproductive for water oxidation – but not for MB degradation – clearly illustrates the prevailing role of bulk properties and mere accessibility of crystal facets that are more important factors than fine-tuning of WOC surface or morphology.

4. Conclusions

The influence of Mo content, particle morphology, surface area and thermal treatment on the photocatalytic activity of hydrothermally synthesized $Bi_{1-x/3}V_{1-x}Mo_xO_4$ ($0.02 < x < 0.15$) materials in MB degradation and water oxidation, respectively, was comprehensively investigated. Catalytic activity results are different from previously reported productive effects of Mo-doping on $BiVO_4$ catalysts obtained from high temperature methods [23].

Neither calcination nor Mo-doping were found to improve the photocatalytic activity of pristine hydrothermally synthesized $BiVO_4$ in MB degradation whilst calcined Mo-free $BiVO_4$ samples showed maximum oxygen production activity. All in all, the adverse effect of Mo substitution, i.e. stabilization of the catalytically less active tetragonal phase of $BiVO_4$, outweighs the benefits of surface acidity and morphology enhancement.

Next, the catalytic tuning potential of TiO_2 and SnO_2 heterojunctions was explored for the above-mentioned photocatalyst series. Pristine $BiVO_4$ and $Bi_{1-x/3}V_{1-x}Mo_xO_4$ ($0.02 < x < 0.15$) were subjected to a mild TiO_2 coating process for the deposition of highly crystalline TiO_2 nanoparticles (around 10 nm). SnO_2-coated catalysts were obtained from brief hydrothermal treatment that led to denser overall surface coating with smaller particles compared to TiO_2. The calcined TiO_2 based composites showed superior performance over pristine $BiVO_4$ and $Bi_{1-x/3}V_{1-x}Mo_xO_4$ in MB degradation. This is in line with the previously described key importance of $BiVO_4$ surface tuning in photocatalytic decomposition reactions for wastewater treatment [42]. The productive effect of TiO_2 coating was less pronounced in O_2 evolution that shows a lower dependence on surface optimization strategies. Finally, SnO_2 coating is applicable for the activity tuning of calcined $BiVO_4$ photocatalysts for MB degradation whilst it is less efficient in combination with Mo doping or for the fine-tuning of O_2 evolution catalysts.

All in all, performance improvement of $BiVO_4$ through Mo incorporation is a challenging multi-parameter process and leaves room for further investigations that are now in progress. The present systematic study demonstrates that the combination of Mo doping and TiO_2 heterojunctions is a promising approach towards the construction of new photocatalysts for visible-light-driven wastewater treatment.

Acknowledgments

This work was supported by the Swiss National Science Foundation (SNSF Professorship PP002-114711/1) and financial support from the University of Zurich is gratefully acknowledged. We are grateful to Prof. Dr. Detlef Günther and Kathrin Hametner (Laboratory of Inorganic Chemistry, ETH Zurich) for LA-ICP-MS analyses. The authors acknowledge support of the Electron Microscopy ETH Zurich, EMEZ, and we thank Dr. Frank Krumeich, EMEZ, for TEM analyses.

References

[1] (a) A. Kudo, Y. Miseki, Chem. Soc. Rev. 38 (2009) 253-278; (b) M. D. Hernández-Alonso, F. Fresno, S. Suárez, J. M. Coronado, Energy Environm. Sci. 2 (2009) 1231-1257.

[2] (a) A. M. Beale, M. T. Le, S. Hoste, G. Sankar, Solid State Sci. 7 (2005) 1141-1148; (b) P. Bégué, R. Enjalbert, J. Galy, A. Castro, Solid State Sci. 2 (2000) 637-653.

[3] (a) Y.-H. Xu, C.-J. Liu, M.-J. Chen, Y.-Q. Liu, Int. J. Nanoparticles 4 (2011) 268-282; (b) H. Kato, M. Hori, R. Konta, Y. Shimodaira, A. Kudo, Chem. Lett. 33 (2004) 1348-1349.

[4] J. D. Bierlein, A. W. Sleight, Solid State Commun. 16 (1975) 69-60.

[5] A. Kudo, K. Omori, H. Kato, J. Am. Chem. Soc. 121 (1999) 11459-11467.

[6] J. B. Liu, K. W. Li, H. Wang, M. K. Zhu, H. Yan, Chem. Phys. Lett. 396 (2004) 429-432.

[7] H. M. Zhang, J. B. Liu, H. Wang, W. X. Zhang, H. Yan, J. Nanopart. Res. 10 (2008) 767 – 774.

[8] W. Liu, L. Cao, G. Su, H. Liu, X. Wang, L. Zhang, Ultrason. Sonochem. 17 (2010) 669-674.

[9] P. Chatchai, Y. Murakami, S. Kishioka, A. Y. Nosaka, Y. Nosaka, Electrochimica Acta 54 (2009) 1147-1152.

[10] M. R. Dolgos, A. M. Paraskos, M. W. Stoltzfus, S. C. Yarnell, P. M. Woodward, J. Solid State Chem. 182 (2009) 1964-1971.

[11] J. Yu, Y. Zhang, A. Kudo, J. Solid State Chem. 182 (2009) 223-228.

[12] P. Chatchai, S. Y. Kishioka, Y. Murakami, A. Y. Nosaka, Y. Nosaka, Electrochimica Acta 55 (2010) 592-596.

[13] D. Zhou, W. G. Qu, C. A. Randall, L. X. Pang, H. Wang, X. G. Wu, J. Guo, G. Q. Zhang, L. Shui, Q. P. Wang, H. C. Liu, X. Yao, Acta Mater. 59 (2011) 1502-1509.

[14] L. Ge, Mater. Lett. 62 (2008) 926-928.

[15] S. Kohtani, J. Hiro, N. Yamamoto, A. Kudo, K. Tokomura, R. Nakagaki, Catal. Commun. 6 (2005) 185-189.

[16] H. Xu, H. Li, C. Wu, J. Chu, Y. Yan, H. Shu, Z. Gu, J. Hazard. Mater. 153 (2008) 877-884.

[17] A. Zhang, J. Zhang, J. Hazard. Mater. 173 (2010) 265.

[18] D. Jing, M. Liu, J. Shi, W. Tang, L. Guo, Catal. Commun. 12 (2010) 264-267.

[19] M.-L. Guan, D.-K. Ma, S.-W. Hu, Y.-J. Chen, S.-M. Huang, Inorg. Chem. 50 (2011) 800-805.

[20] S. J. Hong, S. Lee, J. S. Jang, J. S. Lee, Energy Environm. Sci. 4 (2011) 1781-1787.

[21] J. Su, X.-X. Zou, G.-D. Li, X. Wei, C. Yan, Y.-N. Wang, J. Zhao, L.-J. Zhou, J.-S. Chen, J. Phys. Chem. C 115 (2011) 8064-8071.

[22] W. Yao, J. Ye, J. Phys. Chem. B 110 (2006) 11188 – 11195.

[23] W. Yao, H. Iwai, J. Ye, Dalton Trans. (2008), 1426-1430.

[24] W. Guo, T. Ward, C. Porter, A. Datye, Mater. Res. Bull. 40 (2005) 1371.

[25] M. Cesari, C. Perego, A. Zazzetta, G. Manara, B. Notari, J. Inorg. Nucl. Chem. 33 (1971) 3595-3597.

[26] R. Gruar, C. J. Tighe, L. M. Reilly, G. Sankar, J. A. Darr, Solid State Sci. 12 (2010) 1683-1686.

[27] W. Ueda, K. Asakawa, C.-L. Chen, Y. Moro-oka, T. Ikawa, J. Catal. 101 (1986) 360-368.

[28] M. Hartmanova, M. T. Le, M. Jergel, V. Smatko, F. Kundracik, Russ. J. Electrochem. 45 (2009) 659-667.

[29] M. S. Samant, A. S. Kerkar, S. R. Bharadwaj, S. R. Dharwadkar, J. Alloys Comp. 187 (1992) 373-379.

[30] # (a) Z. Y. Liu, D. D. L. Sun, P. Guo, J. O. Leckie, Nano Lett. 7 (2007) 1081-1085; (b) B. Ma, G. K. L. Goh, T. S. Zhang. J. Ma, Micropor. Mesopor. Mater. 124 (2009) 162-168; (c) Y. Zhou, F. Krumeich, A. Heel, G. R. Patzke, Dalton Trans. 39 (2010) 6043-6048.

[31] (a) D. Koziej, F. Fischer, N. Kranzlin, W. R. Caseri, M. Niederberger, ACS Appl. Mater. & Interf. 1 (2009) 1097-1104; (b) D. P. Macwan, P. N. Dave, S. Charurvedi, J. Mater. Sci. 46 (2011) 3669-3686.

[32] T. H. Ji, F. Yang, J. Y. Zhou, H. Y. Du, J. Y. Sun, Spectrosc. Spectral Anal. 30 (2010) 1944-1947.

[33] Y. Hu, D. Li, Y. Zheng, W. Chen, Y. He, Y. Shao, X. Fu, G. Xiao, Appl. Catal. B 104 (2011) 30 – 36.

[34] Y. Murakami, P. Chatchai, Y. Nosaka, Electrochem. 77 (2009) 44-50.

[35] J. Su, L. Guo, S. Yoriya, C. A. Grimes, Cryst Growth Des. 10 (2010) 865-861.

[36] (a) M. Leoni, T. Confente, P. Scardi, Z. Kristallogr. Suppl. 23 (2006) 249-254; (b) P. Scardi, M. Leoni, J. Appl. Cryst. 39 (2006) 24-31; (c) P. Scardi, Y.H. Dong, M. Leoni, Mat. Sci. Forum 378-381 (2001) 132-139.

[37] W.-J. Yin, S.-H. Wie, M. M. Al-Jassim, J. Turner, Y. Yan, Phys. Rev. B 83 (2011) 155102 1-11.

[38] F. D. Hardcastle, I. E. Wachs, H. Eckert, D. A. Jefferson, J. Solid State Chem. 90 (1991) 194 – 210.

[39] N. Weinstock, H. Schulze, A. Müller, J. Chem. Phys. 59 (1973) 5063-5067.

[40] J. D. Pless, H.-S. Kim, J. P. Smit, X. Wang, P. C. Stair, K. R. Poeppelmeier, Inorg. Chem. 45 (2006) 514-520.

[41] Y. J. Sun, H. J. Liu, X. Wang, X. G. Kong, H. Zhang, Chem. Mater. 13 (2001) 4624-4628.

[42] Y. Zhou, K. Vuille, A. Heel, B. Probst, R. Kontic, G. R. Patzke, Appl. Catal. A 375 (2010) 140-148.